Electrochimica Acta 428 (2022) 140932

Contents lists available at ScienceDirect

Electrochimica Acta

journal homepage: www.journals.elsevier.com/electrochimica-acta

# Pd, Ag and Bi carbon-supported electrocatalysts as electrochemical multifunctional materials for ethanol oxidation and dopamine determination

Luiz Otávio Orzari [a,b], Mônica Helena Marcon Teixeira Assumpção [c], Julio Nandenha [d], Almir Oliveira Neto [d], Luiz Humberto Marcolino Junior [e], Marcio Bergamini [e], Bruno Campos Janegitz [a,*]

[a] Department of Nature Sciences, Mathematics and Education, Federal University of São Carlos, Araras, SP 13600-970, Brazil
[b] Department of Physics, Chemistry and Mathematics, Federal University of São Carlos, Sorocaba, SP 18052-780, Brazil
[c] Center of Nature Sciences, Federal University of São Carlos, Buri, SP 18290-000, Brazil
[d] Instituto de Pesquisas Energéticas e Nucleares (IPEN/CNEN-SP), São Paulo, SP 05508-000, Brazil
[e] Department of Chemistry, Laboratory of Electrochemical sensors (LabSensE), Federal University of Paraná, Curitiba, PR 81531-990, Brazil

ARTICLE INFO

*Keywords:*
Ternary electrocatalysts
Ethanol oxidation
Electrochemical sensor
Dopamine
Multifunctional material

ABSTRACT

This manuscript describes the investigation towards the multifunctional synthesis, characterization, and application of different Pd, Ag and Bi-carbon black supported electrocatalysts in two different fields in electrochemistry: fuel cells and electrochemical sensors. Throughout morphological and electrochemical characterizations, comprising scanning and transmission electron microscopies, X-ray powder diffraction, electrochemical impedance spectroscopy, and cyclic voltammetry techniques, the materials were characterized to better understand their properties towards proposed applications. Afterward, the materials were employed for ethanol oxidation in alkaline media, with investigations by chronoamperometry, cyclic voltammetry, and by closing a direct alkaline fuel cell, which the $Pd_{50}Ag_{45}Bi_{05}/C$ composite presented attractive ethanol catalysis behavior, with a maximum power density of 19.70 mW $cm^{-2}$, at 30.59 mA $cm^{-2}$. Also, the proposed device was applied for dopamine determination by square wave voltammetry. In this sense, two linear behaviors, respectively ranging from 0.2 to 1.0 and 4.0 to 40 μmol $L^{-1}$ were obtained, due to two distinctive mechanisms. This higher activity has been attributed to the synergism among the used metals and proportions contributing to the bifunctional and electronic effects. As synthetic samples investigations were accomplished, data reinforces the proposed material as a possible interfacing composite in electrochemistry.

## 1. Introduction

Through the constant and historical evolution of systems and species, nature presents us with various materials with a multitude of functions, allowing humanity to adapt and develop, building tools and exploring mechanisms and resources in creative ways, such as the use of metal hydroxides in different electrochemical applications [1]; hybrid organic-inorganic compounds, from ancient clays and dyes to modern nano-scaled pigments, medicine, and catalysts [2]. The advantage of such materials relies not solely on their multiple applications, but also on permitting science to discover, interpret and use different properties on already known materials [3,4].

The current constant $CO_2$ emission into the atmosphere, from the use of most fossil fuels, is attributed as the main responsible for the worsening of the greenhouse effect, damaging our entire ecosystem [5,6]. In consideration, science has provided various technological advances in the production of renewable energy, including electrochemical fuel cells [5–10]. Among these, there are types of cells that revolve around the breaking of highly energetic bonds, such as C−C, such as ethanol, which presents itself as a fascinating option for such purpose, and is widely obtained by agriculture, through the cultivation of the *Saccharum* genus species and the principal component obtained by biomass fermentation [7,10].

Two major classes of cells excel at liquid ethanol (ETOH) conversion

* Corresponding author.
*E-mail address:* brunocj@ufscar.br (B.C. Janegitz).

https://doi.org/10.1016/j.electacta.2022.140932
Received 4 March 2022; Received in revised form 11 July 2022; Accepted 28 July 2022
Available online 29 July 2022

to electricity regarding acid and alkaline electrolyte-based systems. Both present interesting options in the matter of cell efficiency, but acid fuel cells bring some problems into consideration, such as the strict control of the aggressive solution and operation procedure, but majorly the amount of Pt – a substantially expensive and scarce metal – needed in its electrodes, for acceptable results. Therefore, some attention was given to alkaline direct ethanol fuel cells (ADEFC), using non-Pt-based electrocatalysts, parameters in which Pd-based approaches greatly outshine other metals [7,10,11].

Pd offers interesting properties, such as relatively lower cost and more abundant obtention than Pt, as well as presenting higher structural stability and activity towards the ethanol oxidation reaction (EOR) in alkaline media than the acid alternative. However, in its pure form, Pd is highly susceptible to surface poisoning, revealing the necessity to modify the catalyst structure for reliable execution [11–14]. In this context, literature brings different investigations about various composites and alloys with the objective of both optimizing the catalytic activity of Pd, as well as making the EOR more viable. Among these, the use of carbon-based substrates can be evidenced, since, in addition to useful electrical conduction, can provide increased surface area for metallic particles [5,6,8–10,14]. In particular, the addition of new components should provide interactions favorable to the increase of active surface area between the elements, further avoiding the poisoning effect [6,15–18]. The addition of Ag and Bi to Pd/C catalysts, for example, can enhance its performance, as suggested by the literature, due to the elimination of intermediate adsorbed species [19] and the Langmuir-Hinshelwood mechanism for surface CO removal [20], among other aspects, such as diminishing the relative material cost when comparing to pure Pd catalysts. Moreover, trimetallic compounds represent promising approaches in several areas, including electroanalysis, as each metal brings various shapes, surface energies, stabilities, and activities, resulting in interesting synergistic effects to be explored [21–25].

Also, carbon nanomaterials, including carbon black, are commonly employed as electrical conductors and performance enhancers in electrochemical sensors [26–30]. Carbon black, especially, can conduct electrons through a variety of mechanisms, according to Medalia [31], including electron tunneling, dielectric breakdown and internal field emission, capacitance, and graphitic-like conduction. Due to its structure and chaotic organization, this latter mechanism is the most prevalent in higher concentrations.

Accordingly, the literature suggests that the architecture of carbon black supported electrocatalysts could also be of interest for the detection of neurological-related catecholamines and hormones, such as dopamine, an important neurotransmitter in mammals, that is recently being correlated to the Huntington's and Parkinson's diseases, with many works [32–34] referring to the molecule as an important probe for molecular diagnostics. Both diseases are of increasing concern in the medical and research fields, especially Huntington, due to their quite recent upbringing of mechanisms [35–37].

An interesting interaction that spontaneously occurs between catecholamines and metallic surfaces is the bidentate chelating and bridging (inner and outer sphere) bonding mechanisms of catechol OH groups with the metallic surface [38–40]. This behavior is especially attributed to the presented metals [39,41,42]. In this work, it was employed in competition with metallic composite, for the formation of $Ag_2O$ on the electrode surface, allowing a lower detection limit for the proposed sensor. Therefore, we propose the synthesis, characterization, and multifunctional application of Pd, Ag, and Bi-supported on carbon black, as interesting electrocatalysts for the EOR in ADEFCs and as a proof-of-concept toward dopamine determination.

## 2. Experimental

### 2.1. Material and reagents

All reagents used in the present study were acquired from the Merck group (Sigma Aldrich) and/or Fluka, in analytical grade. Ultrapure water (Heal Force), with resistivity $> 18.2$ MΩ cm was used in the preparation of all solutions. For the electrochemical characterization of the device, 1.0 mol $L^{-1}$ KOH (pH 13) and 0.1 mol $L^{-1}$ phosphate buffer (Sørensen, different pH values) were used as supporting electrolytes, while the last was also employed for dopamine determination (pH 6.1, defined by literature [43]).

### 2.2. Equipment

All electrochemical analyses were carried on by a potentiostat/galvanostat PGSTAT204 Metrohm (Eco Chemie), managed by Nova 2.1.5 software. A three-electrode system was used, configuring an Ag/AgCl (3.0 mol $L^{-1}$ KCl) as the reference, Pt as counter-electrode, and a modified or bare glassy carbon electrode (GCE) as the working electrode. For all voltammetries, a waiting time of 60 s between the electrode surface and the analyte solution contact was established before the start of the experiments. The electrochemical impedance spectroscopy (EIS) data was obtained in 0.1 mol $L^{-1}$ PB (pH 6.1), with the following parameters: applied potential ($E_{app}$) of −472 mV, potential amplitude of 10 mV, sine waves type throughout all analysis, and 10 frequency increments per decade, in the range of $1.0 \times 10^5$– $1.0 \times 10^{-2}$ Hz. The morphological imaging was performed by Scanning Electron Microscopy (SEM) using a Thermo Scientific Prisma E Scanning Electron Microscope (SEM) with ColorSEM Technology and integrated energy-dispersive X-ray spectroscopy (EDS). Transmission electron microscopy (TEM) images were obtained using a JEOL JEM 1200 instrument at 200 kV (dark-field imaging obtained with the same bright field imaging α). X-ray diffraction (XRD) was performed by a Miniflex II X-ray diffractometer, with a CuKa (λ = 0,15,406 nm) radiation source, in the angular range of 3° to 90°, with a step of 0.02° and 10° $min^{-1}$ analysis time. Fourier transform infrared spectroscopy (FTIR) was obtained by a Tensor II (Bruker), in 4.0 $cm^{-1}$ resolution and transmission mode from 400 to 4000 $cm^{-1}$. An 827 pHmeter (Metrohm) was used in all pH determinations. For experiments in fuel cells, Electrode-Membrane-Electrode (MEAs) assemblies were prepared by hot pressing at 125 °C for 7 min under pressure (225 kgf $cm^{-2}$), using pre-treated Nafion® 117 membranes, placed between the anodic electrocatalysts (Pd/C, $Pd_{50}Ag_{50}$/C, $Pd_{50}Bi_{50}$/C, $Pd_{80}Ag_{15}Bi_{05}$/C, and $Pd_{50}Ag_{45}Bi_{05}$/C) and cathodic electrocatalysts (commercial Pt/C, Basf). The prepared binary and ternary anodes and the cathodes were made with an electrocatalyst mass charge of 1.0 mg(Pd) $cm^{-2}$ [44]. The cell was operated at a temperature of 70 °C. The polarization curves were obtained using an AutoLab PGSTAT302N, also with Nova 2 software for data collection.

### 2.3. Electrocatalysts preparation

All electrocatalysts composites used in this work have 20% of their total mass as metals and the following were synthesized: Pd/C, $Pd_{50}Ag_{50}$/C, $Pd_{50}Bi_{50}$/C, $Pd_{80}Ag_{15}Bi_{05}$/C, and $Pd_{50}Ag_{45}Bi_{05}$/C. These materials were synthesized using a method already found in the literature [5,45]. First, salts of the desired metals (analytical grade) were aliquoted together with the carbon support. Afterward, 0.4 mol $L^{-1}$ HCl was added and the mixture remained under constant stirring for 2 h. Then, concentrated ammonium hydroxide solution was added until pH 11 was reached. Subsequently, an aqueous solution of $NaBH_4$, of concentration whose mass of the reducer corresponded to five times the mass of the total metals, was added to the system in one step, and the mixture remained under constant stirring for another 2 h. The material was then washed with ultrapure water during vacuum filtration, to remove impurities, until reaching pH 7.0. After 4 h of drying in an oven

(60 °C), the materials were ready for use. Finally, electrocatalysts composites were used in the modification of glassy carbon electrodes, for the study of their behavior investigation. Fig. 1 represents the entire process.

### 2.4. Electrode preparation

First, a dispersion of 2.0 mL of the electrocatalysts was prepared with ultra-pure water (1600 μL), isopropyl alcohol (400 μL), Nafion (40 μL), and 12 mg of the composite. Subsequently, a GCE was properly sanded (lemniscate movement) on a velvet surface soaked in concentrated alumina solution and cycled in cyclic voltammetry for 50 scans, in 0.1 mol $L^{-1}$ $H_2SO_4$ solution, with scan rate ($v$) of 50 mV $s^{-1}$, for surface cleaning. After, 6.0 μL of the dispersion was cast on the GCE surface, and following 1.5 h of drying in ambient temperature, the device, entitled $Pd_XAg_YBi_Z$/C/GCE (where *X, Y,* and *Z* represents the percentages of each metal when present) was ready for use.

### 2.5. Parameters optimization

The optimization of the operational parameters for the square wave voltammetry technique (potential step = *s,* pulse amplitude = *a,* and frequency = *f)* was conducted with $2^3$ complete factorial experiments in the following ranges: frequency: 5.0 to 20 Hz, pulse amplitude: 60 to 100 mV and pulse increment: 1.0 to 5.0 mV. These analyzes were performed in the presence of 1.0 μmol $L^{-1}$ dopamine, in a 0.1 mol $L^{-1}$ phosphate buffer solution (pH 6.1, value defined from the literature). Table S1 shows the experimental matrices of the $2^3$ complete factorial experiments (variables, real and coded values, and responses). All experiments were carried out in triplicate and random order [46,47]. In sequence, the two most significant variables (pulse amplitude and frequency) were optimized by applying a $2^2$ central compound arrangement, in the 60 to 100 mV range for pulse amplitude and 2.0 to 10 Hz for the frequency, under the same experimental conditions as described above. The potential step was defined as 5.0 mV, as the experiment with the highest current magnitude occurred with this value. Table S2 presents the matrix for this experiment.

### 2.6. Sample preparation

The dopamine detection by two different mechanisms was performed using the addition and recovery method in synthetic urine. Table S3 shows all the reagents used, as well as their proportions, according to the literature [48–50]. The samples were prepared in phosphate buffer (0.1 mol $L^{-1}$, pH 6.1, with equivalent ionic strength) and spiked with known concentrations of the analyte, ranging from 0.3 to 20 μmol $L^{-1}$. Subsequently, the determination was performed by the addition and recovery method, following both calibration curves, in their respective concentration ranges.

## 3. Results and discussion

### 3.1. Morphological, structural, and electrochemical characterizations

The surface of the modified device with each of the synthesized materials was characterized by SEM, XRD, and TEM techniques, with the data presented in Fig. 2 for the SEM images, Fig. 3 for XRD diffractograms, and Fig. 4 for TEM images. More details about each SEM image can be found in Figs. S1–S5. Through all SEM images, it is possible to note distributed small metallic clusters, with specific structural morphologies varying with the catalyst identity. The Pd/C images reveal that in the prepared conditions, the catalyst film presented disruptions in several places. However, the addition of other metals appears to decrease the frequency of these. $Pd_{50}Ag_{50}$/C electrocatalysts present a high exposition of metallic agglomerations, even more abundantly than Pd/C, throughout the whole external layer. On the other hand, the presence of Bi in these composites conferred wave-like smoother phases, even with smaller concentrations of this element. Both ternary catalysts have shown more localized metallic regions compared to the binary materials, commonly following this wave-like shaped region. The supplementary material includes individual discussions for each electrocatalyst.

In the diffractograms is possible to verify the Pd/C, $Pd_{50}Ag_{50}$/C, $Pd_{50}Bi_{50}$/C, $Pd_{80}Ag_{15}Bi_{05}$/C, and $Pd_{50}Ag_{45}Bi_{05}$/C patterns, to analyze the crystallinity, interactions between the metals, towards the planes are subject to such interactions in the final material. As can be observed in the literature [51], the 2θ = 25° diffraction peak is associated with the presence of graphite (002) of the carbon black support, being its only

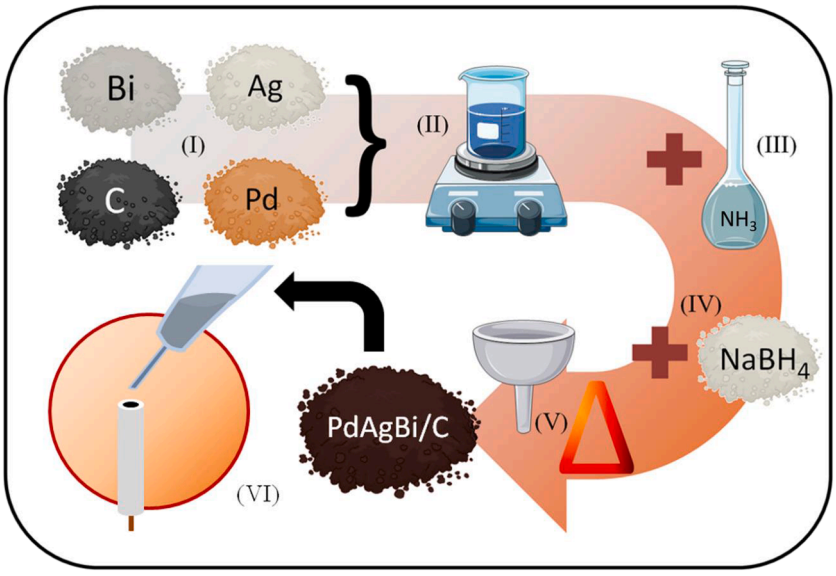


**Fig. 1.** Electrocatalysts preparation scheme. (I) the reagents were aliquoted on an analytical balance (II) for subsequent addition of HCl. (III) After constant stirring, the solution was alkalized with ammonia solution, and (IV) $NaBH_4$ was added for complete reduction. (V) after filtration and thermal processes, (VI) the electrocatalysts are ready for electrode modification.

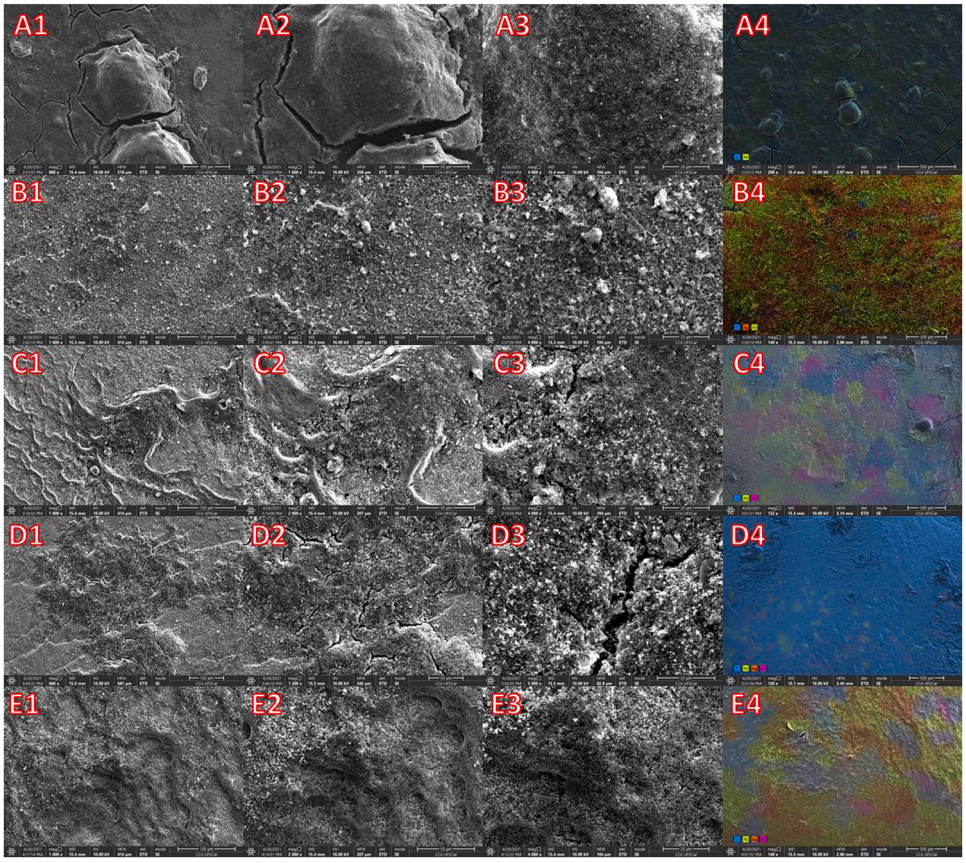


**Fig. 2.** SEM images of (A) Pd/C, (B) $Pd_{50}Ag_{50}$/C, (C) $Pd_{50}Bi_{50}$/C, (D) $Pd_{80}Ag_{15}Bi_{05}$/C and (E) $Pd_{50}Ag_{45}Bi_{05}$/C; 1–3 represents increasing magnifications and 4 presents the EDS imaging.

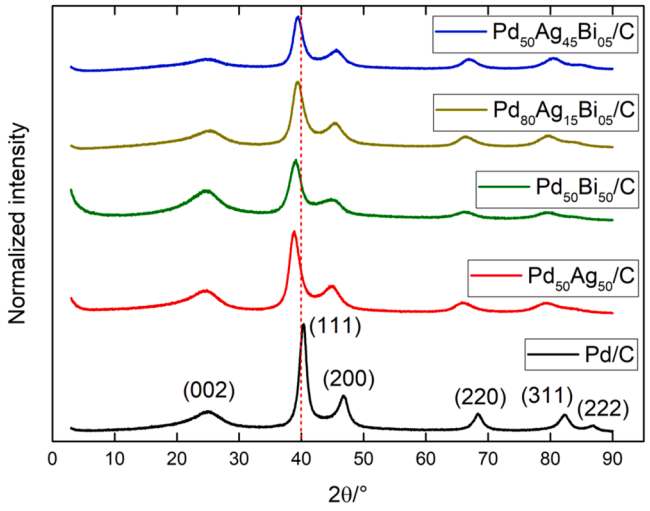


**Fig. 3.** (C) X-ray diffraction patterns of Pd/C (**black**), $Pd_{50}Ag_{50}$/C (**red**), $Pd_{50}Bi_{50}$/C (**green**), $Pd_{80}Ag_{15}Bi_{05}$/C (**gold**) and $Pd_{50}Ag_{45}Bi_{05}$/C (**blue**).

response in the spectrum, since the material is considerably amorphous. For Pd/C, diffraction peaks can be observed in 40, 47, 68, 82 and 86 °, referring to the (111), (200), (220), (311) and (222) planes, the first being the main catalytic plane of the material and all of them corresponding to the face-centered cube structure (FCC) of Pd and its alloys. From the Braggs law for the (220) plane peak, it is possible to estimate the lattice parameter of the system: 0.373 nm, which is in concordance with other Pd/C found in the literature [51,52]. In this case, the average crystallite size is 6.0 nm, calculated by the Scherrer equation for the mean values of each peak. With the addition of Ag and Bi in the composite catalyst, it is possible to note the shift of the above-mentioned peaks toward smaller angles (indicated by the dashed red line), implying the expansion of the FCC structure to accommodate these metals [53]. There is also a decrease in the graphitic character in ternary materials in relation to Pd/C, due to the decrease in 25° peak intensity. The average crystallite size for all the studied materials was also calculated as above: 4.0 nm for $Pd_{50}Ag_{50}$/C, 3.5 nm for $Pd_{50}Bi_{50}$/C, 3.9 nm for $Pd_{50}Ag_{45}Bi_{05}$/C, and 4.1 nm for $Pd_{80}Ag_{15}Bi_{05}$/C.

The TEM is an important tool to identify particle distribution and different structural behavior in a sample, potentially helping to understand different systems behaviors. As previously stated, TEM images of Pd/C, $Pd_{85}Ag_{15}Bi_{05}$/C, and $Pd_{50}Ag_{45}Bi_{05}$/C were presented in Fig. 4. It is possible to observe that, when compared to Pd/C (Fig. 4A), $Pd_{85}Ag_{15}Bi_{05}$/C has a more concentrated metal distribution (Fig. 4B), in the form of bigger agglomerates, as well as having dispersion spots in carbon regions (indicated by dark-field imaging, Fig. 4B4), suggesting a more damaged carbon structure. The $Pd_{50}Ag_{45}Bi_{05}$/C structure (Fig. 4C), however, closely resembles Pd/C, with more homogeneously distributed metals throughout the sample. Also, both dark-field imaging of Pd/C and $Pd_{50}Ag_{45}Bi_{05}$/C indicates electron dispersion spots in regions attributed to metallic particles dispersion.

To understand the catalytic behavior of the investigated materials, we have studied their electrochemical responses in the presence of the alkaline medium. Therefore, cyclic voltammetries were carried out with a 1.0 mol $L^{-1}$ KOH, as these materials are proposed for EOR in alkaline media; in a working potential window of −0.85 to 0.5 V, with a scan rate ($\nu$) of 50 mV $s^{-1}$. Fig. 5A presents these data and all results of EOR were normalized by the specific material Pd mass.

The Pd/C (Fig. 5A, black line, and Fig. S6A) behavior is similar to

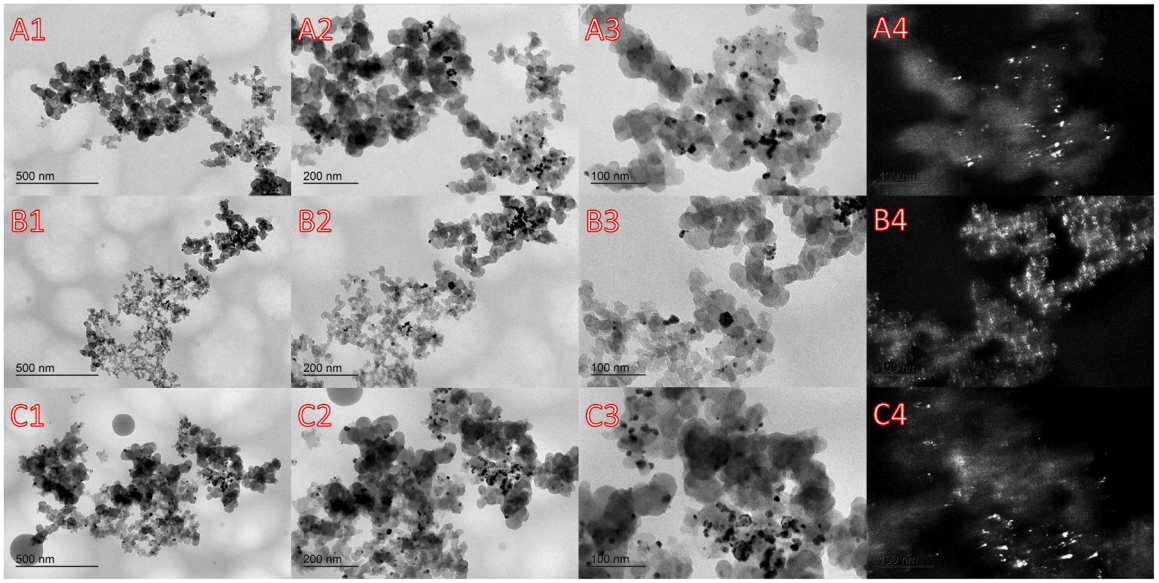


**Fig. 4.** Representative TEM images of Pd/C (**A**), $Pd_{85}Ag_{15}Bi_{05}$/C (**B**) and $Pd_{50}Ag_{45}Bi_{05}$/C (**C**); 1–3 represent increasing magnifications in bright field mode and 4 presents the dark field mode at the highest magnification.

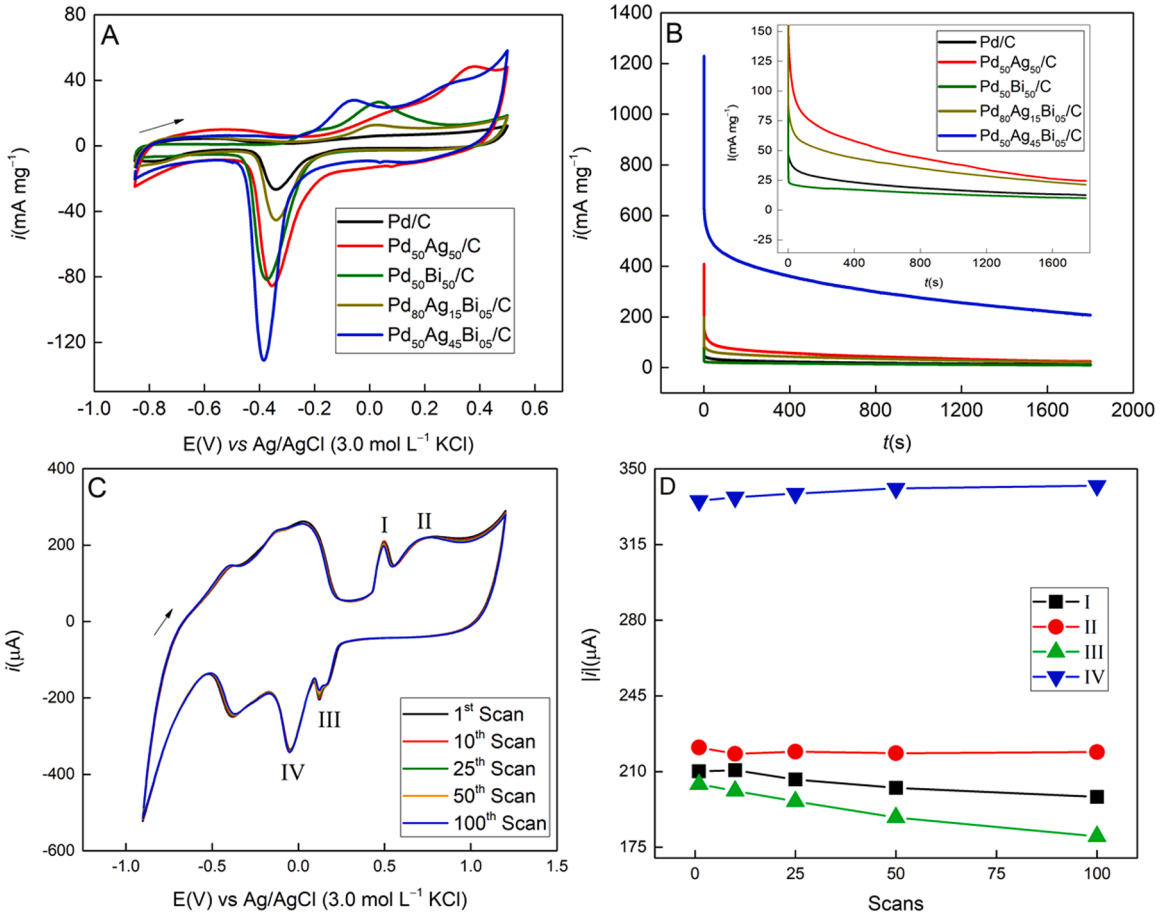


**Fig. 5.** (A) Cyclic voltammograms obtained by GCE modified with Pd/C (**black**), $Pd_{50}Ag_{50}$/C (**red**), $Pd_{50}Bi_{50}$/C (**green**), $Pd_{80}Ag_{15}Bi_{05}$/C (**gold**) and $Pd_{50}Ag_{45}Bi_{05}$/C (**blue**) in presence of 1.0 mol $L^{-1}$ KOH; $\nu = 50$ mV $s^{-1}$; (B) Chronoamperograms obtained by GCE modified with Pd/C (**black**), $Pd_{50}Ag_{50}$/C (**red**), $Pd_{50}Bi_{50}$/C (**green**), $Pd_{80}Ag_{15}Bi_{05}$/C (**gold**) and $Pd_{50}Ag_{45}Bi_{05}$/C (**blue**) in equimolar presence of 1.0 mol $L^{-1}$ ETOH/KOH; $E = -0{,}20$ V, $t = 1800$s; (C) Cyclic voltammograms obtained by $Pd_{50}Ag_{45}Bi_{05}$/C/GCE in 0.1 mol $L^{-1}$ PB (pH 6.1); $\nu = 100$ mV $s^{-1}$; (D) Dispersion plot correlation of $|i|$ vs scan.

others found in the literature [54–56], where it is possible to observe distinct redox processes peaks and regions: although it is not well defined in alkaline media, the hydrogen adsorption region on the Pd surface can be seen between −800 and −500 mV and the PdO formation peaks can be observed at −161 and 22.0 mV, which are subsequently reduced, evidenced by the peak at −337 mV. The $Pd_{50}Ag_{50}$/C behavior (Fig. 5A, red line, and Fig. S6B), presents significant changes when compared to Pd/C. According to the literature [57,58], the presence of Ag near the same percentage as Pd favors the catalytic process in ADEFC. In this configuration, the formation of $Ag_2O$ can be observed near 370 mV and the metallic oxide reduction peak is of increased magnitude compared to Pd/C.

As reported by literature [59], 5.0% of Bi in the catalyst is enough to promote better performance in the EOR, and increasing this percentage could be detrimental to this activity. Fig. 5A (green line and Fig. S6C) presents the electrochemical behavior of $Pd_{50}Bi_{50}$/C, in the previously described conditions and it is possible to note a significant behavior change when compared to the other materials. The metal oxide anodic peaks presented an increased resolution, suggesting a strong surface-oxygen interaction and the catalytic process could be compromised by intense poisoning. Therefore, considering this data and the literature, the proportion of Bi in ternary materials was set at 5.0%.

Two ternary electrocatalysts were synthesized and investigated to further evaluate the Pd to Ag proportional response: $Pd_{80}Ag_{15}Bi_{05}$/C and $Pd_{50}Ag_{45}Bi_{05}$/C. In the first, the logic of maintaining a higher proportion of Pd was sought to assess whether this would be responsible for better catalysis, together with a synergistic effect between all metals. The presence of small quantities of Ag and Bi was enough to cause the presence of an unassuming hydrogen adsorption region in potentials smaller than −500 mV, as can be seen in Fig. 5A (golden line and Fig. S6D), already diverging from the $Pd_{50}Bi_{50}$/C behavior. The voltammogram also presents a single anodic oxide formation peak near 26 mV and the reduction peak is only higher in magnitude than Pd/C. However, by replacing 5.0% of Ag with Bi in $Pd_{50}Ag_{50}$/C, considerable changes emerge (Fig. 5A, blue line, and Fig. S6E): the first anodic peak (60 mV) presented a better resolution, while the second shifted to more negative potentials (from 370 to 305 mV); and the cathodic peak of these processes had the highest current magnitude among all, almost doubling the ones from $Pd_{50}Ag_{50}$/C and $Pd_{50}Bi_{50}$/C. These characteristics could imply a highly active surface if the material proves to be poisoning resistant.

### 3.2. Stability analyses for ETOH oxidation and sensorial applications

For a catalyst to be efficient in a real EOR application, despite facilitating the desired reaction to develop, it also should maintain its activity for longer periods. Accordingly, it is necessary to evaluate the generated current stability, carried out in this work by chronoamperometry. A potential of −0.20 V was applied to all materials for 30 min in 1.0 mol $L^{-1}$ equimolar presence of ETOH/KOH. Fig. 5B presents the obtained chronoamperograms. Table S5 shows the significant data, where a considerable current drop after the first 200 s can be seen, associated with the contribution of the double layer loading and the EOR. For such loading, the distance between the layers is associated with the carbon material, as it is more exposed at the interface. Therefore, as the percentage of this material is the same for all catalysts (80%), the difference in current at the end of the experiment can be associated with the efficiency of the composite for the EOR [60]. The current value (at the end of the chronoamperograms) decreases in the following order: $Pd_{50}Ag_{45}Bi_{05}$/C, $Pd_{50}Ag_{50}$/C, $Pd_{80}Ag_{15}Bi_{05}$/C, Pd/C, and $Pd_{50}Bi_{50}$/C, indicating that $Pd_{50}Ag_{45}Bi_{05}$/C is the most active for this catalytic process among the studied materials. In addition, for this composite, two other properties are also notable with the others: (i) the current decay over time, where the material presents a 6% lower decay rate compared to Pd/C; and (ii) the highest total charge generation, calculated by integrating the chronoamperograms, which is 16 times greater than that of Pd/C. This behavior difference could be explained by different effects: (i) the bifunctional mechanism of EOR catalysis, in which the C−C bond is cleaved and adsorbed in the metallic surface [61]. After, a complex series of reactions can occur, as explored by Dub and Gordon [62], leading to different molecules. As an example, the production of ketones and aldehydes in the metal surface could impair the chemoselectivity of the C=C and C=O cleaving, as only one reaction route could desorb these molecules and it may not be energetically viable for the system to do it; (ii) structural and electronic effects could also be present. As the XRD data suggests that Ag and Bi are added to the Pd FCC structure, effectively forming alloys, the electron transportation of each composite could also be different [63], especially considering the different atomic radii. Taking into account all these aspects and the data collected, the $Pd_{50}Ag_{45}Bi_{05}$/C performance indicates preferable behavior for the EOR, as well as being structurally cohesive for such application, with other investigated composites.

To evaluate the application of the composite in its electrochemical sensing, it is necessary to understand its behavior regarding surface stability. In this context, there is the formation of a few species could be expected for such a purpose, primarily due to the electrolyte/sample composition [64,65]. All the same, if such a phase is complex in nature, with constant compositional variations, the device may not work as an electrochemical sensor, as its optimal working window is impaired by instability. For this purpose, the $Pd_{50}Ag_{45}Bi_{05}$/C/GCE was submitted to 100 successive cyclic voltammetries in 0.1 mol $L^{-1}$ phosphate buffer (pH 6.1), at a scan rate of 100 mV $s^{-1}$, to observe the variation of its electrochemical behavior and Fig. 5C shows the obtained voltammograms for the 1st, 10th, 25th, 50th' and 100th scan.

The presence of four main peaks associated with the presence of metals in this profile can be observed, in addition to the hydrogen adsorption and desorption region. Peaks I and II refer to the formation of Ag and Pd oxides on the device surface. Although, in similar systems, $Ag_2O$ and PdO are commonly formed in regions close to 200 mV [60,66] and 800 mV [64,65], respectively, the presence of $Bi_2O_3$ can infer in the masking of these peaks, since it is formed in the intermediate region between both [12,59]. Thus, it is more appropriate to treat this profile as belonging to the alloy as a whole. Peak III can refer to the counterpart reduction of $Ag_2O$, but in comparable systems, in the literature, this peak is not commonly discussed. Peak IV refers to the complete dissociation of the metal oxides formed [12,59,60,64–66]. Fig. 5D presents the current modulus values for the previous analyzes of the four signals discussed. Among these, only peak III presents a distortion in the profile and a deviation close to 10% ($n = 100$, 5.24% for I, 1.15% for II, 9.73% for III, and 2.88% for IV). Despite being a change in current during the 100 scans, these data suggest that this change is non-significant for the proposed application, as long as the method is standardized. To maintain the profile pattern, this test was repeated before all electrochemical investigations.

### 3.3. Electrochemical impedance spectroscopy

An important analysis regarding the electrochemical performance of the system is the EIS. It provides information that helps in the modeling of the device and the different processes that can occur on its surface, a characteristic that is interesting both for applications in real fuel cells and for the sensing of different species. To carry out this study, the applied potential of −472 mV was selected, as it represents, in 0.1 mol $L^{-1}$ phosphate buffer (pH 6.1) a region of the voltammogram close to the beginning of hydrogen adsorption for all electrocatalysts.

The technique requires a range of potentials in which there is electronic transfer. Therefore, it is estimated that the most suitable potential is the one with the greatest current generation per unit of energy. However, the $Pd_{50}Bi_{50}$/C catalyst has a considerably lower response than the others, limiting the potential to be applied in favor of comparison between all materials, as can be seen in Fig. S7. Fig. 6A and B show, respectively, the Nyquist diagrams and the equivalent circuit for

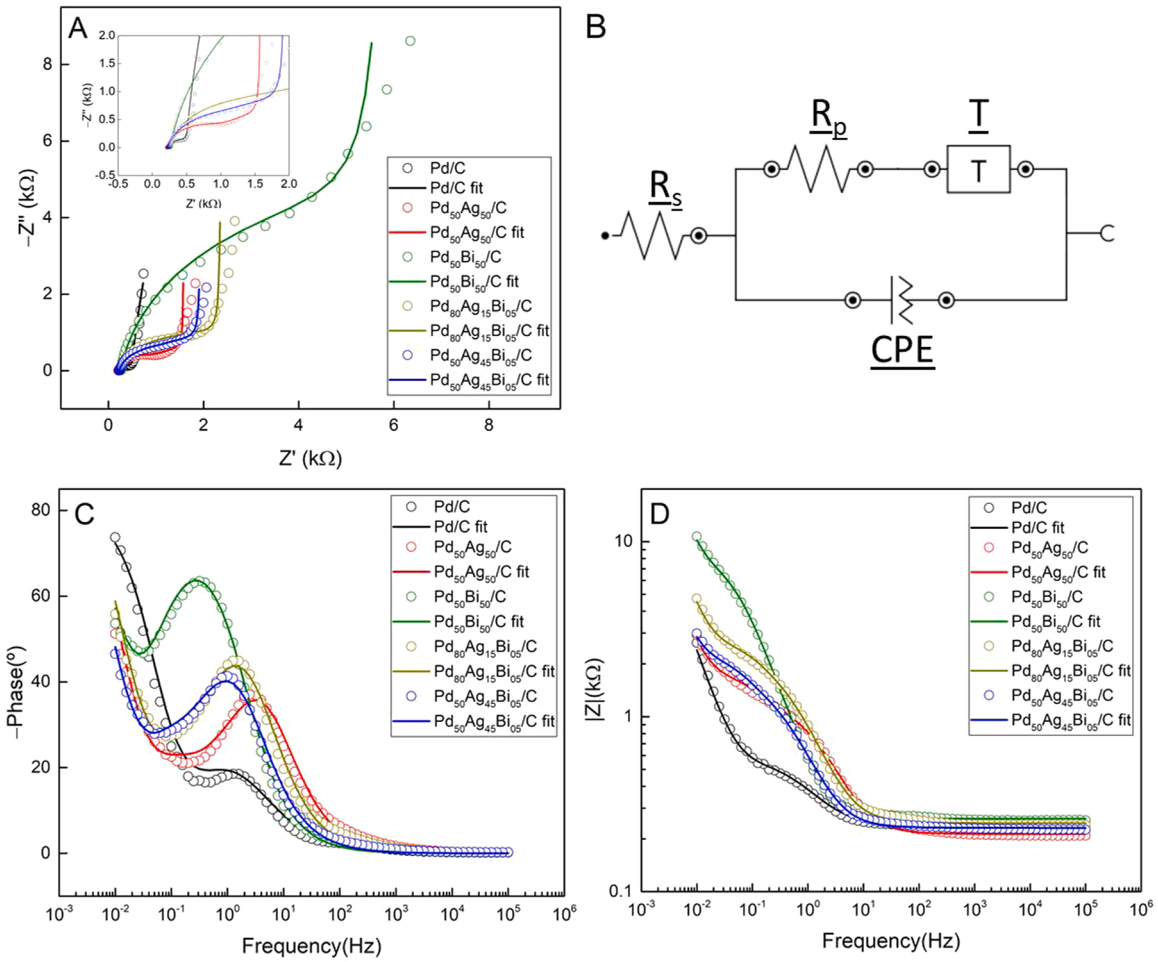


**Fig. 6.** (A) Nyquist diagrams for Pd/C/GCE (**black**), $Pd_{50}Ag_{50}$/C/GCE (**red**), $Pd_{50}Bi_{50}$/C/GCE (**green**), $Pd_{80}Ag_{15}Bi_{05}$/C/GCE (**gold**) and $Pd_{50}Ag_{45}Bi_{05}$/C/GCE (**blue**), in 0.1 mol $L^{-1}$ PB (pH 6.1); $E = -472$ mV; (B) [R([RT]Q)] equivalent circuit; (C and D) Bode diagrams of Pd/C/GCE (**black**), $Pd_{50}Ag_{50}$/C/GCE (**red**), $Pd_{50}Bi_{50}$/C/GCE (**green**), $Pd_{80}Ag_{15}Bi_{05}$/C/GCE (**gold**) and $Pd_{50}Ag_{45}Bi_{05}$/C/GCE (**blue**), in 0.1 mol $L^{-1}$ PB (pH 6.1): (C) −Angle phase and frequency correlation; $E = -472$ mV; (D) Impedance module and frequency correlation; $E = -472$ mV.

the materials, the latter being a modification of the Randles circuit to incorporate diffusion effects of the system. Table S4 includes all data of interest for the circuit of each electrocatalyst: solution resistance (Rs), charge transfer resistance (Rp), and the parameters for the constant phase element (CPE, Y0, and *n*) and the element of Warburg for the open-circuit terminal, T (Y0 and B), where Y0 is the parameter with diffusion coefficient information, calculated by

$$Y0 = \left|\frac{b}{a}\right| \quad (1)$$

where *a* and *b* are the linear and angular coefficient of the Nyquist diagram region that presents an angle of 45°; *n* is the exponential value of the mathematical definition of the CPE, being 1.0 for completely smooth surfaces and decreasing as roughness increases; and B is defined as the square root of the diffusion time, obtained by the equation

$$B = \sqrt{2\pi RC} \quad (2)$$

where *R* and *C* correspond to the [RC] circuit values of the fully capacitive region of the Nyquist diagram (lower frequencies).

The T element arises due to the characteristic absorption of H atoms by the Pd surface over time [65,67], up to the boundary zone (GCE surface), distorting the diffusion region, which the conventional Warburg element no longer comprehends such a system. Bode diagrams for all materials are shown in Fig. 6C and D. As expected, the profiles denote a lower charge transfer for Pd/C since the (111) plane is known to be efficient for such a process and the absence of other metals in the composition can facilitate structuring. It is noteworthy that the materials $Pd_{50}Ag_{50}$/C and $Pd_{50}Ag_{45}Bi_{05}$/C have relatively close charge transfer resistance to each other (771 and 1035 Ω, respectively) indicating that this change in structure has an impact of ≈300 Ω, suggesting effects caused by the greater atomic radius of Bi, as displacements from the plane of catalysis, since Ag has an atomic radius close to that of Pd.

From the phase angle and modulus diagrams of the impedance, it can be seen that the profile of all materials is highly influenced by their surface capacitance presenting the −phase peaks and the difference in inclination of the modulus in the regions of lower frequency. Furthermore, the maximum phase values are smaller than π/2°, increasing in the sequence: Pd/C < $Pd_{50}Ag_{50}$/C < $Pd_{50}Ag_{45}Bi_{05}$/C < $Pd_{80}Ag_{15}Bi_{05}$/C < $Pd_{50}Bi_{50}$/C, also indicating that most process impedances suffer little to mid-term influence of its capacitance, except $Pd_{50}Bi_{50}$/C, which is considerably more affected. $R_s$ value is increasing according to the order $Pd_{50}Ag_{50}$/C < $Pd_{50}Ag_{45}Bi_{05}$/C ≈ Pd/C < $Pd_{80}Ag_{15}Bi_{05}$/C < $Pd_{50}Bi_{50}$/C, implying that the ternary material $Pd_{50}Ag_{45}Bi_{05}$/C possibly has the same charge transfer effects as Pd/C, regardless of its composition and specific mechanisms.

### 3.4. Applications of the trimetallic composite

#### 3.4.1. Ethanol oxidation study

To start understanding the functioning of the catalysts, the half-cells were applied in the evaluation of the catalytic profile for EOR. The oxidation of ETOH in alkaline media can be achieved through different concomitant pathways. In this context, the adsorption involves different species over the Pd surface, mostly leading to three main products: acetate (Eq. 03 to 07), acetaldehyde (Eq. 08 to 10), and carbon dioxide (Eq. (13)). It is important to highlight that the acetaldehyde route is also responsible for the formation of acetate ions, as presented in Eqs. (11) and 12. The C−C breaking to produce $CO_2$ in this latter path is still not well understood in the literature. However, the path is recognized as responsible for catalyst poisoning, due to reactions between adsorbed CO and OH species leading to strongly bonded carbonates over the metal surface [68–70].

*Acetate production pathway*

$$CH_3CH_2OH_{sol} \rightarrow CH_3CH_2OH_{ads} \quad (3)$$

$$OH^- \rightarrow OH_{ads} + e^- \quad (4)$$

$$CH_3CH_2OH_{ads} + 3\ OH_{ads} \rightarrow CH_3CO_{ads} + 3\ H_2O + 3\ e^- \quad (5)$$

$$CH_3CO_{ads} + OH_{ads} \rightarrow CH_3COOH \quad (6)$$

$$CH_3COOH + OH^- \rightarrow \mathbf{CH_3COO^-} + H_2O \quad (7)$$

*Acetaldehyde and acetate production pathway*

$$2\ OH^- \rightarrow 2\ OH_{ads} + 2\ e^- \quad (8)$$

$$CH_3CH_2OH_{sol} + OH_{ads} \rightarrow CH_3CH_2O^{\bullet} + H_2O \quad (9)$$

$$CH_3CH_2O^{\bullet} + OH_{ads} \rightarrow \mathbf{CH_3CHO} + H_2O \quad (10)$$

$$CH_3CHO + 2\ OH^- \rightarrow CH_3COOH + H_2O + 2\ e^- \quad (11)$$

$$CH_3COOH + OH^- \rightarrow \mathbf{CH_3COO^-} + H_2O \quad (12)$$

*Carbon dioxide production pathway*

$$CO_{ads} + 2\ OH_{ads} + 3OH^- \rightarrow \mathbf{CO_2} + H_2O + e^- \quad (13)$$

Therefore, 1.0 mol $L^{-1}$ ETOH was added to the systems described in Section 3.1. Cyclic voltammograms were obtained in the same working window, also at 50 mV $s^{-1}$. Fig. 7A presents all the cyclic voltammograms obtained, and, as before, each case will be discussed individually.

The profile presented by Pd/C presents a standard for evaluating the performance of other materials. Fig. 7A (black line) and S8A show such a profile, where it is possible to see the ethanol oxidation peak at 103 mV, of 135 mA $mg^{-1}$, with an onset potential ($E_{op}$) equal to −391 mV, obtained by the abscissa of the point of tangents interpolation between non-Pharadaic and Pharadaic regions. It is also observed that in the reverse (cathodic) direction, there is an anodic process related to the desorption of species produced by the adsorption of ETOH on the

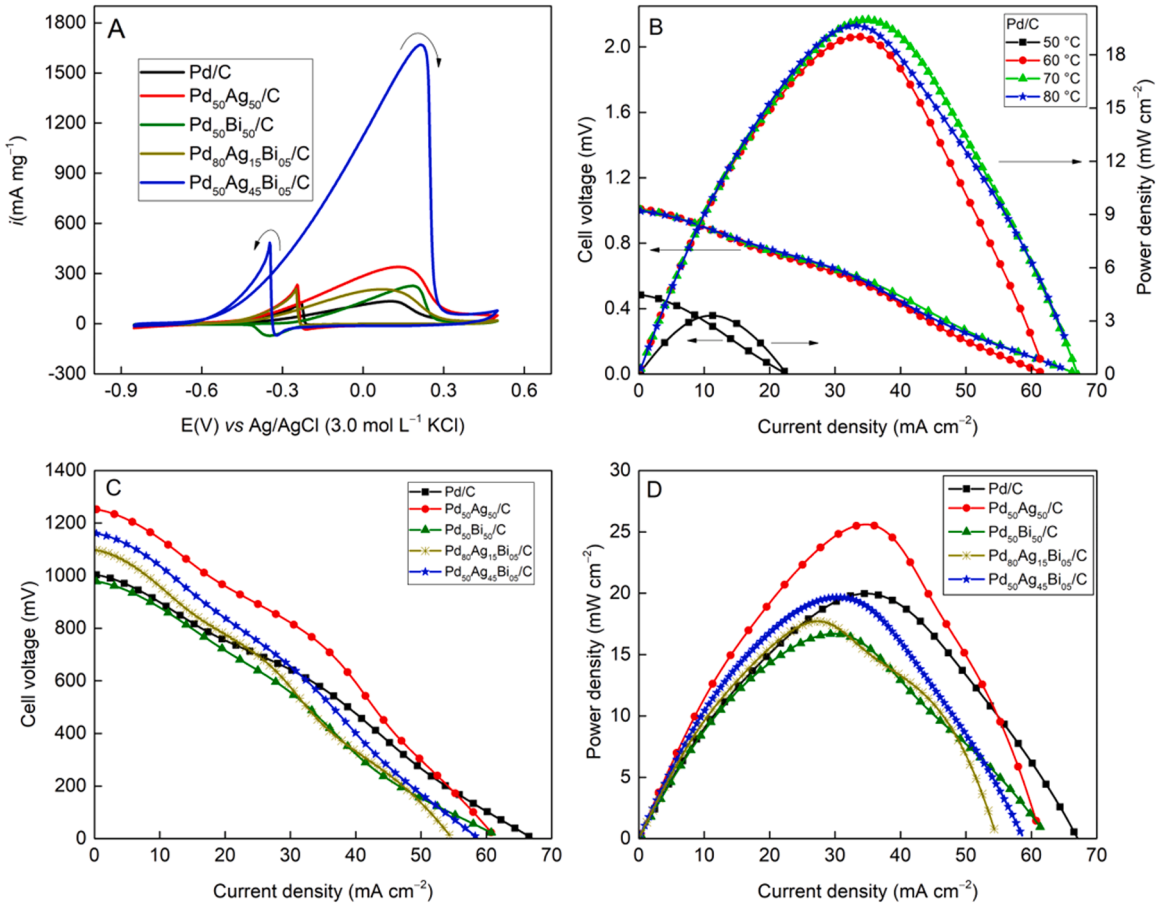


**Fig. 7.** (A) Cyclic voltammograms obtained by GCE modified with Pd/C (**black**), $Pd_{50}Ag_{50}$/C (**red**), $Pd_{50}Bi_{50}$/C (**green**), $Pd_{80}Ag_{15}Bi_{05}$/C (**gold**) and $Pd_{50}Ag_{45}Bi_{05}$/C (**blue**) in equimolar presence of 1.0 mol $L^{-1}$ ETOH/KOH; $\nu = 50$ mV $s^{-1}$; (B) Polarization curves: potential and power density vs current density, of a 5.0 $cm^2$ ADEFC, operating at 50, 60, 70 and 80 °C, using Pd/C as anodic electrocatalyst, and commercial Pt/C as cathodic electrocatalyst; anodic and cathodic metal loading of 1.0 $mg_{(Pd)}$ $cm^{-2}$, with *Nafion*® 117 membrane, fed with 1.0 mL $min^{-1}$ 2.0 mol $L^{-1}$ ETOH in KOH 1.0 mol $L^{-1}$, mass flow rate of 150 mL $min^{-1}$ of $O_2$. Polarization curves of (C) potential vs current density and (D) power density vs current density, of a 5.0 $cm^2$ ADEFC, operating at 70 °C, using Pd/C, $Pd_{50}Ag_{50}$/C, $Pd_{50}Bi_{50}$/C, $Pd_{80}Ag_{15}Bi_{05}$/C and $Pd_{50}Ag_{45}Bi_{05}$/C as anodic electrocatalyst, and commercial Pt/C as cathodic electrocatalyst; anodic and cathodic metal loading of 1.0 $mg_{(Pd)}$ $cm^{-2}$, with *Nafion*® 117 membrane, fed with 1.0 mL $min^{-1}$ 2.0 mol $L^{-1}$ ETOH in KOH 1.0 mol $L^{-1}$, mass flow rate of 150 mL $min^{-1}$ of $O_2$.

material surface.

The obtained $Pd_{50}Ag_{50}$/C profile (Fig. 7A, red line; and S8B) demonstrates that the addition of Ag, in these proportions, gives a considerable increase to the catalyst performance. An oxidation peak is observed at 131 mV, with a peak current equal to 340 mA $mg^{-1}$, as well as an $E_{op}$ of −411 mV. The discussed potentials were shifted in opposite directions, indicating that the process started earlier (lower energy barrier) and peaked later (increased overall process time duration), both indicators of an enhanced system. For the cathodic step, the detachment generated an anodic peak of magnitude closer to that of the anodic peak, having a current gain of 1.5 times and a 29% current difference between these processes.

As discussed earlier, the amount of Bi atoms in the catalyst could provide impairments in the catalysis, and, as Fig. 7A (green line) and S8C show, $Pd_{50}Bi_{50}$/C is not an efficient material for this application. The oxidation peak is present at 185 mV, with a magnitude of 226 mA $mg^{-1}$ and an $E_{op}$ of −225 mV. In the cathodic scan, the material does not present the desorption profile, having a cathodic peak at −347 mV, which can indicate a severe poisoning of the device [63]. This material presents a 67% current gain, but these other factors make it impossible to use this metal proportion for the proposed application.

Fig. 7A (golden line) and S8D show the profile obtained for the first ternary catalyst, $Pd_{80}Ag_{15}Bi_{05}$/C, where an anodic peak at 68 mV is present, with a current generation of 206 mA $mg^{-1}$ and an $E_{op}$ of −403 mV. The anodic process in cathodic scanning shows a peak, in which there were no significant losses in intensity, indicating a low tendency to poisoning. Like $Pd_{50}Ag_{50}$/C, this has an $E_{op}$ value slightly shifted to more negative potentials, as well as a current gain of 52%. Although the peak potential has shifted to more negative potentials, this material presents interesting results, having its efficiency inferior only to $Pd_{50}Ag_{50}$/C.

The second ternary catalyst, $Pd_{50}Ag_{45}Bi_{05}$/C, has its profile shown in Fig. 7A (blue line) and S8E. It is observed that the material provided a peak potential of 219 mV, with a magnitude equivalent to 1669 mA $mg^{-1}$ and $E_{op}$ of −486 mV, and the peak from the cathodic scan demonstrates a 3.5-fold current loss. However, the gain in the generated current for the oxidation of ethanol surpasses that of other materials, being equivalent to 12.4 times greater than that generated by Pd/C. In addition, both potentials described above indicate opposite shifts, also foreshadowing an enhanced process concerning Pd/C, possibly due to structural and electronic effects.

To better evaluate the applicability of the studied materials, ADEFCs experiments were performed, evaluating the power and current density obtained closer to real conditions. In this regard, Fig. 7B shows the polarization curves, in different temperatures (50, 60, 70, and 80 °C) for the electrochemical oxidation of ethanol by Pd/C, in presence of 2.0 mol $L^{-1}$ ETOH, in 1.0 mol $L^{-1}$ KOH in different temperatures. This step is essential to guarantee optimal system output energy-wise. As can be noted, the temperature of 70 °C was the most efficient, presenting the best reaction kinetics. For this reason, this temperature was selected for the experiments of all electrocatalysts in this study.

The polarization curves obtained in a 5.0 $cm^2$ ADEFC, operating at 70 °C, using the anodic electrocatalysts Pd/C, $Pd_{50}Ag_{50}$/C, $Pd_{50}Bi_{50}$/C, $Pd_{80}Ag_{15}Bi_{05}$/C, and $Pd_{50}Ag_{45}Bi_{05}$/C are illustrated in Fig. 7C and D. Among these, $Pd_{50}Ag_{50}$/C, $Pd_{50}Ag_{45}Bi_{05}$/C, and $Pd_{80}Ag_{15}Bi_{05}$/C electrocatalysts showed open-circuit potential values equal to ~1250, 1161, and 1097 mV, respectively, all higher, in comparison, to the Pd/C electrocatalyst (997 mV). The open-circuit potential value of the $Pd_{50}Bi_{50}$/C electrocatalyst was 972 mV (Fig. 7C). The $Pd_{50}Ag_{50}$/C electrocatalyst showed a maximum power density value for the EOR of 25.65 mW $cm^{-2}$ at 34.67 mA $cm^{-2}$ and higher compared to the other electrocatalysts: Pd/C and $Pd_{50}Ag_{45}Bi_{05}$/C demonstrated approximate efficiency (19.97 mW $cm^{-2}$ ≈ 19.70 mW $cm^{-2}$, at 35.53 mA $cm^{-2}$ and 30.59 mA $cm^{-2}$, respectively); The maximum power density of $Pd_{50}Bi_{50}$/C equals 16.66 mW $cm^{-2}$ in 30.05 mA $cm^{-2}$ and of $Pd_{80}Ag_{15}Bi_{05}$/C corresponds to 17.75 mW $cm^{-2}$ at 27.21 mA $cm^{-2}$, as seen in Fig. 7D.

As already discussed, these experiments corroborated that the addition of 50% Ag content in Pd/C electrocatalyst promoted the electrocatalytic activity for the electrochemical oxidation of ethanol in the alkaline medium, with $Pd_{50}Ag_{50}$/C presenting a maximum power density of 25.65 mW $cm^{-2}$ in alkaline medium. This value is superior in comparison to the other synthesized electrocatalysts. As also explored, the addition of Ag is expected to enhance the catalysis possibly due to a combination of active area and the presence of oxygenated species. This fact is due to a synergistic effect of the presence of surface oxides and structural changes caused by the dissolution of Ag; while the inclusion of Bi over the Pd structure,when in higher concentrations, can cover active sites at the main metal surface, preventing the oxidation of ethanol. These effects were in agreement with the data observed in the chronoamperometry for both bimetallic catalysts.

For the ternary electrocatalysts, the lower maximum power density of $Pd_{80}Ag_{15}Bi_{05}$/C demonstrates that the removal of these 20% Pd severely hinders the efficiency of the catalyst in more realistic situations. However, the $Pd_{50}Ag_{45}Bi_{05}$/C obtained data also suggests that the substitution of 5% Ag for Bi, at $Pd_{50}Ag_{50}$/C, presented material with close behavior to that of the pure Pd/C. Even though at 70 °C, this ternary electrocatalyst does not hold to its higher semi-cell performance, the experiment put forward the question of electrocatalysts cost-benefit. To produce 100 mg of Pd/C, US$7.62 in precursor metallic salts (Pd nitrate (II) dihydrate, Sigma Aldrich, the price obtained in 07/07/2022) must be applied in its synthesis. By dividing the maximum power density of this electrocatalyst by its metal cost, we obtain the value of 2.62 mW $cm^{-2}$ US$$^{-1}$. Submitting $Pd_{50}Ag_{45}Bi_{05}$/C to the same analysis, this electrocatalyst gives us a value of 5.09 mW $cm^{-2}$ US$$^{-1}$, 1.94 times higher maximum power density per dollar invested in the material production, for the EOR in alkaline media. Therefore, all these analyses endorse that the ternary electrocatalyst $Pd_{50}Ag_{45}Bi_{05}$/C can be an alternative to pure Pd electrocatalysts.

### 3.4.2. Dopamine determination study

Due to the efficiency demonstrated in the catalysis of ETOH, the catalyst $Pd_{50}Ag_{45}Bi_{05}$/C was selected as the modifier for the electrochemical sensor, supporting the idea of multiple functions. Firstly, it is necessary to know the electrochemical profile of the device in the presence of the desired analyte. Therefore, the modified electrode was applied for the detection of dopamine with the cyclic voltammetry technique, in a 0.1 mol $L^{-1}$ phosphate buffer solution, in the presence of 10 μmol $L^{-1}$ of the neurotransmitter, at $\nu$ 100 mV $s^{-1}$, as shown in Fig. 8A. Dopamine was selected as the analyte and proof-of-concept due to its relationship with several neurodegenerative maladies, especially Huntington's and Parkinson's diseases, in addition to its range of data found in the literature and its easy acquisition by the laboratory.

As can be seen, the presence of this molecule has three main effects: (I) the increase in current in the hydrogen adsorption region, which may be related to the release of protons; (II) the presence of an anodic peak at 122 mV, referring to the direct oxidation of dopamine hydroxyls; (III) the decrease in the magnitude of the peaks of first metallic oxidative interaction, especially for the peak associated with the formation of $Ag_2O$ in Section 3.1. The technique chosen for more sensitive dopamine detection was square wave voltammetry, and to obtain better peak resolution and reliable data, optimizations were necessary. Therefore, data from the screening experiments described in Section 2.5. are presented in Table S6, as well as the effects calculated among the parameters ($f$ = X1, $a$ = X2, and $s$ = X3) and the response obtained.

Analyzing the results, it is possible to notice that the effects provided by variable X3 ($s$) are considerably less significant than the others, even if in its confidence interval it does not exceed a null value, it permeates ~1.0% of influence in the sum of squared effects. Therefore, the optimal value for $s$ was defined as 5.0 mV, which is the value when the highest peak current magnitude was obtained during the experiments. Thus, the two remaining parameters were subjected to $2^2$ central composite arrangement analyses. From the responses in Table S3, it was possible to

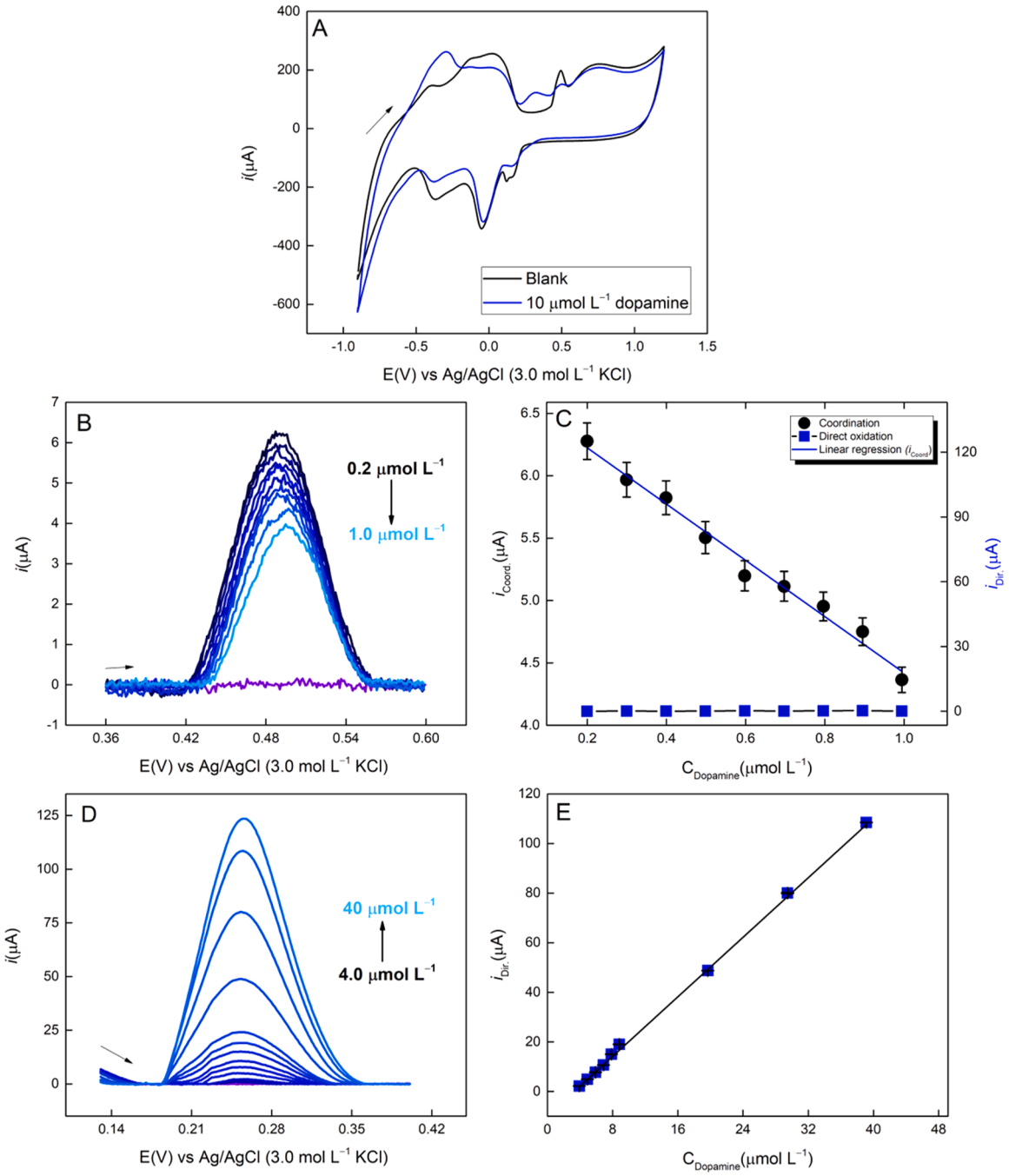


**Fig. 8.** (A) Cyclic voltammograms obtained by $Pd_{50}Ag_{45}Bi_{05}$/C/GCE in absence (**black**) and presence (**blue**) of 10 μmol $L^{-1}$ dopamine, in 0.1 mol $L^{-1}$ PB (pH 6.1); $v = 100$ mV $s^{-1}$; (B) Square wave voltammograms obtained by $Pd_{50}Ag_{45}Bi_{05}$/C/GCE in presence of varying concentrations of dopamine, in 0.1 mol $L^{-1}$ PB (pH 6.1); $s = 5.0$ mV, $a = 100$ mV, $f = 6.0$ Hz; (C) Dispersion plot of $i_{Dir.}$ vs $C_{Dopamine}$ (■) and $i_{Coord.}$ vs $C_{Dopamine}$ (●) correlations; (D) Square wave voltammograms obtained by $Pd_{50}Ag_{45}Bi_{05}$/C/GCE in presence of varying concentrations of dopamine, in 0.1 mol $L^{-1}$ PB (pH 6.1); $s = 5.0$ mV, $a = 100$ mV, $f = 6.0$ Hz; (E) Dispersion plot of $i_{Dir.}$ vs $C_{Dopamine}$ correlation.

generate surface response surface and contour curve for the peak current behavior with $a \times f$, in the presence of dopamine, as shown in Fig. S9.

With the analysis of these data, it is possible to determine the superposition region that is expected a greater sensitivity for the determination of dopamine. Therefore, the defined optimal parameters are $s = 5.0$ mV, $a = 100$ mV and $f = 6.0$ Hz, denoted by a four-pointed star in the figure. The pH (6.1) was defined according to the literature [43,71]. Several experiments were carried on with the optimized parameters, in presence of variable dopamine concentrations: 0.20, 0.30, 0.40, 0.50, 0.60, 0.70, 0.80, 0.90, 1.0, 2.0, 3.0, 4.0, 5.0, 6.0, 7.0, 8.0, 9.0, 10, 20, 30 and 40 μmol $L^{-1}$, which data are present in Figs. S10, 8B to D. The former presents the whole behavior, in which can be seen that the anodic peak corresponding to the formation of metal oxides (487 mV) and there is a decrease in magnitude as the dopamine concentration increases, even before the electrochemical signal of the molecule oxidation (262 mV) is visible. This behavior remains linear until the direct oxidation peak of the analyte becomes visible. The literature brings several works that explore the formation of stable complexes of different metals with the catechol group [38–40], such as the work of Oliveira et al. [72], which used Ni hexacyanoferrate anchored at Ni nanoparticles. The presence of rifampicin led to a decrease in the faradic process, suggesting an interaction between the antibiotic and metallic

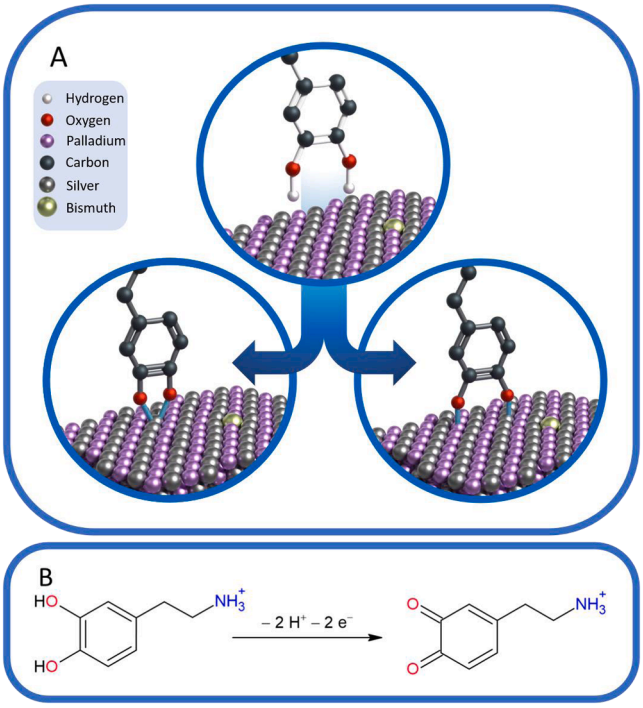


**Fig. 9.** (A) possible coordination of the catechol group with the metallic surface. (B) The direct oxidation reaction of dopamine.

ions.

Therefore, Fig. 9A presents our proposed mechanism involving the device surface and the dopamine molecule. This event occurs due to the ease of coordination of the oxygens present in the catechol group with the metallic surface, both of which can be directly bonded to a single atom or a 1:1 bond (O:M). This mechanism can occur at room temperatures, does not destabilize the resonance of the molecule, and is presented especially with Ag [41] and Pd [42]. The literature suggests [39] that this complex can be formed with Bi, but works involving this element have not been found. As its percentage in this material is considerably lower than that of other metals, it is estimated that this bond is not prioritized. Fig. 9B also shows the dopamine direct oxidation mechanism, involving 2 protons and 2 electrons.

With delimitation of the linear regions, two analytical curves were constructed, one for each mechanism. The relationship between the signals of the metal and the dopamine coordination can be seen in more detail in Fig. 8B and C. The peak decays linearly between 0.2 and 1.0 μmol $L^{-1}$, corresponding to the linear equation $i_{Coord.}$ (μA) = −2.25 × $C_{Dopamine}$ (μmol $L^{-1}$) + 6.68, with $R^2$ = 0.990. The limit of detection (LOD) was calculated based on 3 times the standard deviation of the linear regression, divided by the calibration curve slope [73], and the value obtained was 0.14 μmol $L^{-1}$. Fig. 8D and E show the linear range for the calibration curve of the direct dopamine oxidation peak, suitable between 4.0 and 40 μmol $L^{-1}$, corresponding to the linear equation $i_{Dir.}$ (μA) = 3.00 × $C_{Dopamine}$ (μmol $L^{-1}$) – 9.85, with $R^2$ = 0.999. For this process, the LOD was calculated by 3.0 times the standard deviation of 10 blank analyses, divided by the analytical curve slope [73], and is equal to 0.035 μmol $L^{-1}$.

To evaluate the device in more complex samples, synthetic urine was synthesized with the addition of known concentrations of dopamine. The tests were performed according to the experimental conditions of the analytical curve and Table 1 shows the obtained data, which range from 92.0 to 114% for the dopamine direct oxidation peak and from 92.6 to 110% for the coordination process peak.

The performance of the PdAgBi/C/GCE for dopamine determination has been compared to similar works in literature, as presented in

**Table 1**
Determination of dopamine in synthetic urine samples by the direct oxidation peak of dopamine and the peak of dopamine-metal complexes.

| Dopamine direct oxidation signal | | | |
|---|---|---|---|
| Sample | Add(μmol $L^{-1}$) | Detected(μmol $L^{-1}$) | Recovery% |
| A | 4.00 | 4.46 | 114 |
| B | 8.00 | 8.17 | 102 |
| C | 20.0 | 18.4 | 92.0 |
| Dopamine-metal complexation signal | | | |
| Sample | Add (μmol $L^{-1}$) | Detected (μmol $L^{-1}$) | Recovery% |
| A | 0.300 | 0.329 | 110 |
| B | 1.00 | 0.926 | 92.6 |
| C | 0.700 | 0.757 | 109 |

Table S7. It is observed that the selected works present similarities in the employed materials and/or methodology. As can be noted, this work presents itself as an interesting approach for both functions, being relatively close in the linear range, LOD and sensibility when compared to other works.

## 4. Conclusion

This paper seeks to contribute to the idea of producing multifunctional materials due to their expanding usefulness, by presenting ternary electrocatalysts designed for such a function, showing promising materials for ETOH oxidation and dopamine electrochemical sensing. The electrocatalysts synthesis is relatively easy and with considerable efficiency. EOR analysis suggests that the $Pd_{50}Ag_{45}Bi_{05}$/C material has potential for this application, presenting a current and charge production of, respectively, 12.4 and 16.5 times greater than that of Pd/C (observed in chronoamperometry and cyclic voltammetries), with a relatively low rate of poisoning, which was attributed to the bifunctional and electronic effects, due to the presence of oxide species observed in voltammetry and the shift distinguished in XRD peaks, indicative of the alloy formation. The analyses in real ADEFCs (70 °C) demonstrated that even though the $Pd_{50}Ag_{45}Bi_{05}$/C, cannot compete with $Pd_{50}Ag_{50}$/C in maximum power density, its behavior was similar to that of Pd/C, but with almost half the material cost production, further cementing its attractive capabilities. Although the formation profile of metal-associated peaks appears, at first, to limit the device working potential range (by overlapping peaks), the data presented suggest a linear interaction of the surface with dopamine in a given region. Thus, it was possible to construct two calibration curves: the first, related to this mechanism, starting from 0.2 to 1.0 μmol $L^{-1}$, resulting in a recovery in a urine sample synthetic between 92.6 and 110%; and the second, related to the dopamine oxidation peak, covers the range from 4.0 to 40 μmol $L^{-1}$ and presents recoveries between 92.0 and 114% in the same sample. With these data, it is also suggested the practicality of preparing materials for two different research fronts, rarely studied together.

## CRediT authorship contribution statement

**Luiz Otávio Orzari:** Investigation, Methodology, Validation, Data curation, Writing – review & editing. **Mônica Helena Marcon Teixeira Assumpção:** Conceptualization, Data curation, Writing – review & editing. **Julio Nandenha:** Investigation, Methodology, Validation, Data curation. **Almir Oliveira Neto:** Investigation, Methodology, Validation, Data curation. **Luiz Humberto Marcolino Junior:** Conceptualization, Data curation, Writing – review & editing. **Marcio Bergamini:** Conceptualization, Data curation, Writing – review & editing. **Bruno Campos Janegitz:** Conceptualization, Visualization, Supervision, Project administration, Resources, Funding acquisition, Writing – review & editing.

## Declaration of Competing Interest

The authors declare that they have no known competing financial interests or personal relationships that could have appeared to influence the work reported in this paper.

## Data availability

Data will be made available on request.

## Acknowledgments

The authors of this work acknowledge the Fundação de Amparo à Pesquisa do Estado de São Paulo (FAPESP), Brazil (Grants# 2019/23342–0, 2017/21097–3), Coordenação de Aperfeiçoamento de Pessoal de Nível Superior (CAPES) (financial code 001 and CAPES 09/2020 Epidemias 88887.504861/2020–00) and the Conselho Nacional de Desenvolvimento Científico e Tecnológico (CNPq, 303338/2019–9), Brazil for all the financial support.

## Supplementary materials

Supplementary material associated with this article can be found, in the online version, at doi:10.1016/j.electacta.2022.140932.

## References

[1] E.G. Neiva, M.M. Oliveira, M.F. Bergamini, L.H. Marcolino, A.J.G. Zarbin, One material, multiple functions: graphene/Ni $(OH)_2$ thin films applied in batteries, electrochromism and sensors, Sci. Rep. 6 (2016) 1–14.
[2] L. Nicole, C. Laberty-Robert, L. Rozes, C.J.N. Sanchez, Hybrid materials science: a promised land for the integrative design of multifunctional materials, Nanoscale 6 (2014) 6267–6292.
[3] R.F. Gibson, A review of recent research on mechanics of multifunctional composite materials and structures, Compos. Struct. 92 (2010) 2793–2810.
[4] P. Ragesh, V.A. Ganesh, S.V. Nair, A.S. Nair, A review on 'self-cleaning and multifunctional materials, J. Mater. Chem. A 2 (2014) 14773–14797.
[5] M.H. Assumpção, R.M. Piasentin, P. Hammer, R.F. De Souza, G.S. Buzzo, M. C. Santos, E.V. Spinacé, A.O. Neto, J.C.M. Silva, Oxidation of ammonia using PtRh/C electrocatalysts: fuel cell and electrochemical evaluation, Appl. Catal. B 174 (2015) 136–144.
[6] J.C.M. Silva, M.H. Assumpção, P. Hammer, A.O. Neto, E.V. Spinacé, E.A. Baranova, Iridium− rhodium nanoparticles for ammonia oxidation: electrochemical and fuel cell studies, ChemElectroChem 4 (2017) 1101–1107.
[7] E. Antolini, Catalysts for direct ethanol fuel cells, J. Power Sources 170 (2007) 1–12.
[8] E. Antolini, Platinum-based ternary catalysts for low temperature fuel cells: part I. Preparation methods and structural characteristics, Appl. Catal. B 74 (2007) 324–336.
[9] M. Assumpção, J. Nandenha, G. Buzzo, J. Silva, E. Spinacé, A. Neto, R. De Souza, The effect of ethanol concentration on the direct ethanol fuel cell performance and products distribution: a study using a single fuel cell/attenuated total reflectance–Fourier transform infrared spectroscopy, J. Power Sources 253 (2014) 392–396.
[10] S.G. Silva, M.H. Assumpção, R.F. Souza, G.S. Buzzo, E.V. Spinacé, A.O. Neto, J.C. M. Silva, Electrochemical and fuel cell evaluation of PtIr/C electrocatalysts for ethanol electrooxidation in alkaline medium, Electrocatalysis 4 (2014) 438–444.
[11] Z. Liang, T. Zhao, J. Xu, L. Zhu, Mechanism study of the ethanol oxidation reaction on palladium in alkaline media, Electrochim. Acta 54 (2009) 2203–2208.
[12] B. Cermenek, J. Ranninger, B. Feketeföldi, I. Letofsky-Papst, N. Kienzl, B. Bitschnau, V. Hacker, Novel highly active carbon supported ternary PdNiBi nanoparticles as anode catalyst for the alkaline direct ethanol fuel cell, Nano Res. 12 (2019) 683–693.
[13] S.M. Mostashari, R.A. Dehkharghani, M. Farsadrooh, F. Afshar-Taromi, Engineering three-dimensional superstructure of Pd aerogel with enhanced performance for ethanol electrooxidation, J. Mol. Liq. (2022), 119363.
[14] A. Brouzgou, E. Gorbova, Y. Wang, S. Jing, A. Seretis, Z. Liang, P. Tsiakaras, Nitrogen-doped 3D hierarchical ordered mesoporous carbon supported palladium electrocatalyst for the simultaneous detection of ascorbic acid, dopamine, and glucose, Ionics 25 (2019) 6061–6070. Kiel.
[15] M. Götz, H. Wendt, Binary and ternary anode catalyst formulations including the elements W, Sn and Mo for PEMFCs operated on methanol or reformate gas, Electrochim. Acta 43 (1998) 3637–3644.
[16] A. Lima, C. Coutanceau, J.M. Léger, C. Lamy, Investigation of ternary catalysts for methanol electrooxidation, J. Appl. Electrochem. 31 (2001) 379–386.
[17] K. Neyerlin, G. Bugosh, R. Forgie, Z. Liu, P. Strasser, Combinatorial study of high-surface-area binary and ternary electrocatalysts for the oxygen evolution reaction, J. Electrochem. Soc. 156 (2009) B363–B369.
[18] N.V. Long, Y. Yang, C.M. Thi, N. Van Minh, Y. Cao, M. Nogami, The development of mixture, alloy, and core-shell nanocatalysts with nanomaterial supports for energy conversion in low-temperature fuel cells, Nano Energy 2 (2013) 636–676.
[19] M.M. Tusi, N.S. Polanco, S.G. da Silva, E.V. Spinacé, A.O. Neto, The high activity of PtBi/C electrocatalysts for ethanol electro-oxidation in alkaline medium, Electrochem. Commun. 13 (2011) 143–146.
[20] T. Jurzinsky, C. Cremers, K. Pinkwart, J. Tübke, On the influence of Ag on Pd-based electrocatalyst for methanol oxidation in alkaline media: a comparative differential electrochemical mass spectrometry study, Electrochim. Acta 199 (2016) 270–279.
[21] N. Basavegowda, T.K. Mandal, K.H. Baek, Bimetallic and trimetallic nanoparticles for active food packaging applications: a review, Food Bioprocess Technol. 13 (2020) 30–44.
[22] M. Ding, J. Chen, M. Jiang, X. Zhang, G. Wang, Ultrathin trimetallic metal–organic framework nanosheets for highly efficient oxygen evolution reaction, J. Mater. Chem. 7 (2019) 14163–14168.
[23] T. Gunji, F. Matsumoto, Electrocatalytic activities towards the electrochemical oxidation of formic acid and oxygen reduction reactions over bimetallic, trimetallic and core–shell-structured Pd-based materials, Inorganics 7 (2019) 36.
[24] N. Du, C. Wang, X. Wang, Y. Lin, J. Jiang, Y. Xiong, Trimetallic TriStar nanostructures: tuning electronic and surface structures for enhanced electrocatalytic hydrogen evolution, Adv. Mater. 28 (2016) 2077–2084.
[25] M. Salamanca, Y.E. Licea, A. Echavarría, A.C. Faro Jr, L.A. Palacio, Hydrothermal synthesis of new wolframite type trimetallic materials and their use in oxidative dehydrogenation of propane, Phys. Chem. Chem. Phys. 11 (41) (2009) 9583–9591.
[26] F. Arduini, A. Amine, C. Majorani, F. Di Giorgio, D. De Felicis, F. Cataldo, D. Moscone, G. Palleschi, High performance electrochemical sensor based on modified screen-printed electrodes with cost-effective dispersion of nanostructured carbon black, Electrochem. Commun. 12 (2010) 346–350.
[27] D.C. de Souza, L.O. Orzari, P.R. de Oliveira, C. Kalinke, J.A. Bonacin, O. Malaspina, R.C.F. Nocelli, B.C. Janegitz, Electrochemical sensor based on beeswax and carbon black thin biofilms for determination of paraquat in apis mellifera honey, Food Anal. Methods 14 (2021) 606–615.
[28] T.A. Silva, F.C. Moraes, B.C. Janegitz, O. Fatibello-Filho, Electrochemical biosensors based on nanostructured carbon black: a review, J. Nanomater. (2017) 2017.
[29] A. Brouzgou, C.L. Vecchio, V. Baglio, A.S. Aricò, Z.X. Liang, A. Demin, P. Tsiakaras, Glucose electrooxidation reaction in presence of dopamine and uric acid over ketjenblack carbon supported PdCo electrocatalyst, J. Electroanal. Chem. 855 (2019), 113610.
[30] X. Zhang, J. Zheng, Hollow carbon sphere supported Ag nanoparticles for promoting electrocatalytic performance of dopamine sensing, Sens. Actuators B 290 (2019) 648–655.
[31] A.I. Medalia, Electrical conduction in carbon black composites, Rubber Chem. Technol. 59 (1986) 432–454. Singap World Sci.
[32] A. Baranwal, P. Chandra, Clinical implications and electrochemical biosensing of monoamine neurotransmitters in body fluids, *in vitro, in vivo*, and *ex vivo* models, Biosens. Bioelectron. 121 (2018) 137–152.
[33] A. Yildirim, M. Bayindir, Turn-on fluorescent dopamine sensing based on *in situ* formation of visible light emitting polydopamine nanoparticles, Anal. Chem. 86 (2014) 5508–5512.
[34] Q.J. Lu, X.G. Chen, D. Liu, C.Y. Wu, M.L. Liu, H.T. Li, Y.Y. Zhang, S.Z. Yao, Synergistic electron transfer effect-based signal amplification strategy for the ultrasensitive detection of dopamine, Talanta 182 (2018) 428–432.
[35] G.P. Bates, R. Dorsey, J.F. Gusella, M.R. Hayden, C. Kay, B.R. Leavitt, M. Nance, C. A. Ross, R.I. Scahill, R. Wetzel, Huntington disease, Nat. Rev. Dis. Prim. 1 (2015) 1–21.
[36] U. Rüb, J.P. Vonsattel, H. Heinsen, H.W. Korf, The neuropathology of huntington's disease: classical findings, recent developments and correlation to functional neuroanatomy, Adv. Anat. Embryol. Cell Biol. 217 (2015) 7–23.
[37] E.R. Fisher, M.R. Hayden, Multisource ascertainment of Huntington disease in Canada: prevalence and population at risk, Mov. Disord. 29 (2014) 105–114.
[38] M. Ata, Y. Liu, I. Zhitomirsky, A review of new methods of surface chemical modification, dispersion and electrophoretic deposition of metal oxide particles, J. RSC Adv. 4 (2014) 22716–22732.
[39] J. Guo, Y. Ping, H. Ejima, K. Alt, M. Meissner, J.J. Richardson, Y. Yan, K. Peter, D. Von Elverfeldt, C.E. Hagemeyer, Engineering multifunctional capsules through the assembly of metal–phenolic networks, Angew. Chem. Int. Ed. 53 (2014) 5546–5551.
[40] Z. Xu, Mechanics of metal-catecholate complexes: the roles of coordination state and metal types, Sci. Rep. 3 (2013) 2914.
[41] A.C. Rossi-Fernández, L.A. Meier, N.F. Domancich, N.J. Castellani, Electric field effects on the adsorption of dopamine species on Ag (111): DFT investigation of interaction mechanism, ChemistrySelect 5 (2020) 4728–4739.
[42] G. Bauer, M. Nieger, D. Gudat, Heterobimetallic catechol-phosphine complexes with palladium and a group-13 element: structural flexibility and dynamics, Dalton Trans. 43 (2014) 8911–8920.
[43] L.O. Orzari, R. Cristina de Freitas, I. Aparecida de Araujo Andreotti, A. Gatti, B. C. Janegitz, A novel disposable self-adhesive inked paper device for electrochemical sensing of dopamine and serotonin neurotransmitters and biosensing of glucose, Biosens. Bioelectron. 138 (2019), 111310.
[44] J.C.M. Silva, G.S. Buzzo, R.F.B. De Souza, E.V. Spinacé, A.O. Neto, M. Assumpção, Enhanced electrooxidation of ethanol using Pd/C+ $TiO_2$ electrocatalysts in alkaline media, Electrocatalysis 6 (2015) 86–91.

[45] R.C. de Freitas, L.O. Orzari, P.R. de Oliveira, B.C. Janegitz, Pd and Ag binary nanoparticles supported on carbon black and tapioca for nitrite electrochemical detection, J. Electrochem. Soc. 168 (2021), 117518.
[46] B.B. Neto, I.S. Scarminio, R.E. Bruns, Como fazer experimentos-: pesquisa e desenvolvimento na ciência e na indústria, Bookman Editora, 4th ed., (2010) 2010.
[47] F.C. Vicentini, L.C.S. Figueiredo-Filho, B.C. Janegitz, A. Santiago, E.R. Pereira-Filho, O. Fatibello-Filho, Planejamento fatorial e superfície de resposta: otimização de um método voltamétrico para a determinação de ag(i) empregando um eletrodo de pasta de nanotubos de carbono, Quím. Nova 34 (2011) 825–830.
[48] M. Baccarin, F.A. Santos, F.C. Vicentini, V. Zucolotto, B.C. Janegitz, O. Fatibello-Filho, Electrochemical sensor based on reduced graphene oxide/carbon black/chitosan composite for the simultaneous determination of dopamine and paracetamol concentrations in urine samples, J. Electroanal. Chem. 799 (2017) 436–443.
[49] A.M. Campos, P.A. Raymundo-Pereira, C.D. Mendonça, M.L. Calegaro, S. A. Machado, O.N. Oliveira Jr, Size control of carbon spherical shells for sensitive detection of paracetamol in sweat, saliva, and urine, ACS Appl. Nano Mater. 1 (2018) 654–661.
[50] P.A. Raymundo-Pereira, F.M. Shimizu, D. Coelho, M.H. Piazzeta, A.L. Gobbi, S. A. Machado, O.N. Oliveira Jr, A nanostructured bifunctional platform for sensing of glucose biomarker in artificial saliva: synergy in hybrid Pt/Au surfaces, Biosens. Bioelectron. 86 (2016) 369–376.
[51] C.A. Martins, P.S. Fernández, H.E. Troiani, M.E. Martins, A. Arenillas, G.A. Camara, Agglomeration and cleaning of carbon supported palladium nanoparticles in electrochemical environment, Electrocatalysis 5 (2014) 204–212.
[52] R. Lamber, S. Wetjen, N.I. Jaeger, Size dependence of the lattice parameter of small palladium particles, Phys. Rev. B 51 (1995) 10968.
[53] A. Neto, S. da Silva, G. Buzzo, R. de Souza, M. Assumpção, E. Spinacé, J. Silva, Ethanol electrooxidation on PdIr/C electrocatalysts in alkaline media: electrochemical and fuel cell studies, Ionics 21 (2015) 487–495. Kiel.
[54] S. Liu, W. Xiao, J. Wang, J. Zhu, Z. Wu, H. Xin, D. Wang, Ultralow content of Pt on Pd–Co–Cu/C ternary nanoparticles with excellent electrocatalytic activity and durability for the oxygen reduction reaction, Nano Energy 27 (2016) 475–481.
[55] L. An, Y. Chen, J. Shi, J. Cao, B. Liu, J. Yang, Oxygen Reduction activity and stability of composite Pdx/Co-nanofilms/C electrocatalysts in acid and alkaline media, Front. Chem. 6 (2018) 1–10.
[56] H. Meng, D. Zeng, F. Xie, Recent development of Pd-based electrocatalysts for proton exchange membrane fuel cells, Catalysts 5 (2015) 1221–1274.
[57] S.T. Nguyen, H.M. Law, H.T. Nguyen, N. Kristian, S. Wang, S.H. Chan, X. Wang, Enhancement effect of Ag for Pd/C towards the ethanol electro-oxidation in alkaline media, Appl. Catal. B 91 (2009) 507–515.
[58] C. Bianchini, P.K. Shen, Palladium-based electrocatalysts for alcohol oxidation in half cells and in direct alcohol fuel cells, Chem. Rev. 109 (2009) 4183–4206.
[59] A.O. Neto, M.M. Tusi, N.S. de Oliveira Polanco, S.G. Da Silva, M.C. Dos Santos, E. V. Spinace, PdBi/C electrocatalysts for ethanol electro-oxidation in alkaline medium, Int. J. Hydrog. Energy 36 (2011) 10522–10526.
[60] G. Li, L. Jiang, Q. Jiang, S. Wang, G. Sun, Preparation and characterization of PdxAgy/C electrocatalysts for ethanol electrooxidation reaction in alkaline media, Electrochim. Acta 56 (2011) 7703–7711.
[61] S. Mondal, C.R. Raj, Electrochemical dealloying-assisted surface-engineered Pd-based bifunctional electrocatalyst for formic acid oxidation and oxygen reduction, ACS Appl. Mater. Interfaces 11 (2019) 14110–14119.
[62] P.A. Dub, J.C. Gordon, Metal–ligand bifunctional catalysis: the “accepted” mechanism, the issue of concertedness, and the function of the ligand in catalytic cycles involving hydrogen atoms, ACS Catal. 7 (2017) 6635–6655.
[63] A.S. Bandarenka, M.T.M. Koper, Structural and electronic effects in heterogeneous electrocatalysis: toward a rational design of electrocatalysts, J. Catal. 308 (2013) 11–24.
[64] P.K. Shen, C. Xu, Alcohol oxidation on nanocrystalline oxide Pd/C promoted electrocatalysts, Electrochem. Commun. 8 (2006) 184–188.
[65] S. Mahapatra, J. Datta, Characterization of Pt-Pd/C electrocatalyst for methanol oxidation in alkaline medium, Int. J. Electrochem. (2011), 2011.
[66] S.T. Nguyen, Y. Yang, X. Wang, Ethanol electro-oxidation activity of Nb-doped-$TiO_2$ supported PdAg catalysts in alkaline media, Appl. Catal. B 113 (2012) 261–270.
[67] L.L. Fang, Q. Tao, M.F. Li, L.W. Liao, D. Chen, Y.X. Chen, Determination of the real surface area of palladium electrode, Chin. J. Chem. Phys. 23 (2010) 543–548.
[68] A.O. Neto, S.G. Da Silva, G.S. Buzzo, R.F.B. De Souza, M. Assumpção, E.V. Spinacé, J.C.M. Silva, Ethanol electrooxidation on PdIr/C electrocatalysts in alkaline media: electrochemical and fuel cell studies, Ionics 21 (2015) 487–495. Kiel.
[69] M. Assumpção, J. Nandenha, G.S. Buzzo, J.C.M. Silva, E.V. Spinacé, A.O. Neto, R.F. B. De Souza, The effect of ethanol concentration on the direct ethanol fuel cell performance and products distribution: a study using a single fuel cell/attenuated total reflectance–Fourier transform infrared spectroscopy, J. Power Sources 253 (2014) 392–396.
[70] A.N. Geraldes, D.F. Da Silva, E.S. Pino, J.C.M. Da Silva, R.F.B. De Souza, P. Hammer, E.V. Spinacé, A.O. Neto, M. Linardi, M.C. Dos Santos, Ethanol electro-oxidation in an alkaline medium using Pd/C, Au/C and PdAu/C electrocatalysts prepared by electron beam irradiation, Electrochim. Acta 111 (2013) 455–465.
[71] L.O. Orzari, F.A. Santos, B.C. Janegitz, Manioc starch thin film as support of reduced graphene oxide: a novel architecture for electrochemical sensors, J. Electroanal. Chem. 823 (2018) 350–358.
[72] P.R. Oliveira, A.F. Schibelbain, E.G.C. Neiva, A.J.G. Zarbin, L.H. Marcolino-Junior, M.F. Bergamini, Nickel hexacyanoferrate supported at nickel nanoparticles for voltammetric determination of rifampicin, Sens. Actuators B 260 (2018) 816–823.
[73] A. Shrivastava, V.B. Gupta, Methods for the determination of limit of detection and limit of quantitation of the analytical methods, Chron. Young Sci. 2 (2011) 21–25.